

# Crack-front model for adhesion of soft elastic spheres with chemical heterogeneity

Antoine Sanner<sup>a,b</sup>, Lars Pastewka<sup>a,b</sup>

<sup>a</sup>*Department of Microsystems Engineering, University of Freiburg, Georges-Köhler-Allee 103, 79110 Freiburg, Germany*

<sup>b</sup>*Cluster of Excellence livMatS, Freiburg Center for Interactive Materials and Bioinspired Technologies, University of Freiburg, Georges-Köhler-Allee 105, 79110 Freiburg, Germany*

---

## Abstract

Adhesion hysteresis can be caused by elastic instabilities that are triggered by surface roughness or chemical heterogeneity. However, the role of these instabilities in adhesion hysteresis remains poorly understood because we lack theoretical and numerical models accounting for realistic roughness. Our work focuses on the adhesion of soft elastic spheres with low roughness or weak heterogeneity, where the indentation process can be described as a Griffith-like propagation of a nearly circular external crack. We discuss how to describe the contact of spheres with chemical heterogeneity that leads to fluctuations in the local work of adhesion. We introduce a variational first-order crack-perturbation model and validate our approach using boundary-element simulations. The crack-perturbation model faithfully predicts contact shapes and hysteretic force-penetration curves, provided that the contact perimeter remains close to a circle and the contact area is simply connected. Computationally, the crack-perturbation model is orders of magnitude more efficient than the corresponding boundary element formulation, allowing for realistic heterogeneity fields. Furthermore, our crack-front formulation clarifies the connection of adhesion hysteresis to classic theories on pinning of elastic lines.

*Keywords:* adhesion and adhesives, hysteresis, elastic material, contact mechanics, crack propagation and arrest

---

## 1. Introduction

Soft materials stick to rough surfaces if the elastic energy needed to conform to surface roughness is small compared to the surface energy gained by contact (Fuller and Tabor, 1975; Briggs and Briscoe, 1977; Persson and Tosatti, 2001). In an indentation experiment with such materials, the force needed to break the contact is often higher than the force measured during indentation (Chen et al., 1991). This observation contradicts expectations from classical theories on smooth surfaces (Johnson et al., 1971) and theories for rough contacts that assume the contact follows thermodynamic equilibrium

---

*Email addresses:* antoine.sanner@imtek.uni-freiburg.de (Antoine Sanner), lars.pastewka@imtek.uni-freiburg.de (Lars Pastewka)

*Preprint submitted to Elsevier*

*August 17, 2021*

(Persson and Tosatti, 2001; Persson, 2002a,b). This *adhesion hysteresis* can be caused by several mechanisms like viscoelasticity, molecular rearrangements and elastic instabilities. Recent work indicates that in some cases, elastic instabilities triggered by surface roughness play the dominant role (Kesari et al., 2010; Dalvi et al., 2019). Details of how roughness gives rise to elastic instabilities remain poorly understood, mainly because we lack theoretical models accounting for realistic surface roughness.

In this paper, we discuss how to describe the contact of elastic spheres with chemical heterogeneity, local fluctuations in the work of adhesion, using a first-order crack-perturbation model. Understanding the hysteresis caused by quenched disorder in the work of adhesion is a first step towards a general model for geometrically rough surfaces. Our model will permit efficient numerical simulations of realistic system sizes and clarify the link between adhesive contact mechanics and classic theories on pinning of elastic lines.

Depending on the compliance of the elastic material, hysteresis arises from disconnected patches snapping in and out of contact or depinning instabilities in the motion of the contact perimeter, the crack front. Brute-force numerical methods like the boundary element method (BEM) can capture these different regimes of instabilities (Medina and Dini, 2014; Dapp and Müser, 2015; Carbone et al., 2015; Deng and Kesari, 2017; Wang et al., 2021). However, for soft materials it is challenging to sufficiently discretize the adhesive neck (or crack tip) and at the same time include a representative amount of surface roughness (Wang et al., 2021). Insufficient discretization in boundary element models can additionally lead to “lattice trapping”, that causes artificial pinning of the crack front alike physical lattice trapping in atomic crystal (Thomson et al., 1971).

More coarse-grained models either concentrate on the two opposite limits of very low contact fraction or full contact. Asperity models describe surface roughness as a set of spherical peaks with random heights (Greenwood and Williamson, 1966; Fuller and Tabor, 1975), that dissipate energy during snap in and out of contact instabilities (Zappone et al., 2007; Wei et al., 2010; Greenwood, 2017; Deng and Kesari, 2019; Violano and Afferrante, 2021). This type of approximation breaks down when asperities coalesce and a larger fraction of the surface comes into contact. In the limit of small roughness and low stiffness, the contact area is simply connected. In that limit, the surface roughness causes energy barriers that pin the crack front and the crack front dissipates energy during depinning instabilities. This phenomenon has to date only been studied on one-dimensional roughness (Guduru, 2007; Guduru and Bull, 2007; Kesari et al., 2010; Kesari and Lew, 2011; Carbone et al., 2015).

The pinning of a crack front by quenched disorder in the work of adhesion (or equivalently, the fracture toughness) is better understood (Gao and Rice, 1989; Schmittbuhl et al., 1995; Xia et al., 2012; Démery et al., 2014; Xia et al., 2015; Chopin et al., 2015; Ponson, 2016; Lebihain et al., 2021). An essential step towards this understanding was Rice’s description of a semi-infinite crack as an elastic line with long-range elasticity (Rice, 1985a). This equation belongs to the class of elastic interfaces pinned by a random field and the current understanding on fracture of heterogeneous media benefited from works in other fields (Larkin and Ovchinnikov, 1979; Fisher, 1983; Robbins and Joanny, 1987; Middleton, 1992; Amaral et al., 1995; Zhou, 2000; Rosso and Krauth, 2002; Tanguy and Vettorel, 2004; Rosso et al., 2007).

Rice’s first-order perturbation was applied to several geometries with finite sizes (Lazarus, 2011; Patinet et al., 2013). To our knowledge, this perturbation approach

was never applied to the contact of spheres or similar indenters, except recently by Argatov (2021) to investigate the effect of indenter ellipticity on the pull-off force. Crack perturbation is a promising approach to understand how surface roughness affects adhesion hysteresis in indentation experiments where the contact area is simply connected. The first step towards this end is to understand how the adhesion hysteresis depends on the geometry and strength of quenched disorder in the work of adhesion.

In this paper, we discuss how to describe the contact of spheres with fluctuating work of adhesion as a perturbation from the homogeneous, perfectly circular contact, as described by the Johnson-Kendall-Roberts (JKR) theory (Johnson et al., 1971; Barthel, 2008). The perturbation relies on the first functional derivative of the stress intensity factor derived by Gao and Rice (1987a). We describe below that there is no unique way to extrapolate the elastic response of the elastic line. In the past either the stress intensity factor (Gao and Rice, 1989; Fares, 1989) or the energy release rate (Bonamy et al., 2008; Ponson and Bonamy, 2010; Patinet et al., 2013; Chopin et al., 2015; Ponson, 2016) was linearly extrapolated. We here propose a third equation that ensures that the crack front possess an elastic potential and therefore constitutes a variational approach to crack perturbation. In order to validate our model and to discriminate between different variants of the perturbation, we compare the crack-perturbation models to finely discretized BEM simulations. Figure 1 illustrates schematically the two types of models used in this paper.

## 2. Problem definition

We consider the contact of a sphere (to be exact, a paraboloid) adhering an elastic half-space at a fixed rigid body penetration  $\Delta$ . This case can be mapped to the contact of two spheres with the same composite radius  $R$  and contact modulus  $E'$  (Johnson, 1985). When only one half-space deforms,  $E' = E/(1 - \nu^2)$ , where  $E$  is Young's modulus and  $\nu$  is Poisson's ratio. Fracture mechanics typically considers the contact of two elastic half-spaces where  $E' = E/2(1 - \nu^2)$ . We assume the contact is frictionless and consider only vertical displacements.

The equilibrium contact area minimizes the total energy  $\Pi = \Pi_{\text{mech}} + \Pi_{\text{surf}}$ . The mechanical energy  $\Pi_{\text{mech}}$  contains the elastic strain energy  $U_{\text{el}}$  and the potential of external forces. The surface energy  $\Pi_{\text{surf}}$  results from adhesive interactions. We consider the limit of infinitesimally short interaction range (JKR-limit), where

$$\Pi_{\text{surf}} = \int_{A_c} dx dy w(x, y). \quad (1)$$

$A_c$  is the contact area and the work of adhesion  $w(x, y)$  depends on the position  $(x, y)$ . Note that the work of adhesion is the same for a receding crack (indentation) as for an opening crack (retraction), i.e. there is no *intrinsic* hysteresis in the work of adhesion.

Once nondimensionalized using distinct vertical and lateral length units, the JKR contact is parameter free (Muller et al., 1980; Maugis, 2010; Müser, 2014). We present our numerical results in nondimensional units (Maugis, 2010) and indicate by an asterisk\* when quantities are normalized. Specifically, lengths along the surface of the half-space (e.g., the contact radius) are normalized by  $(3\pi w_m R^2/4E')^{1/3}$ , lengths in vertical direction (e.g., displacements) by  $(9\pi^2 w_m^2 R^2/16E'^2)^{1/3}$  and normal forces by  $\pi w_m R$ .  $w_m$

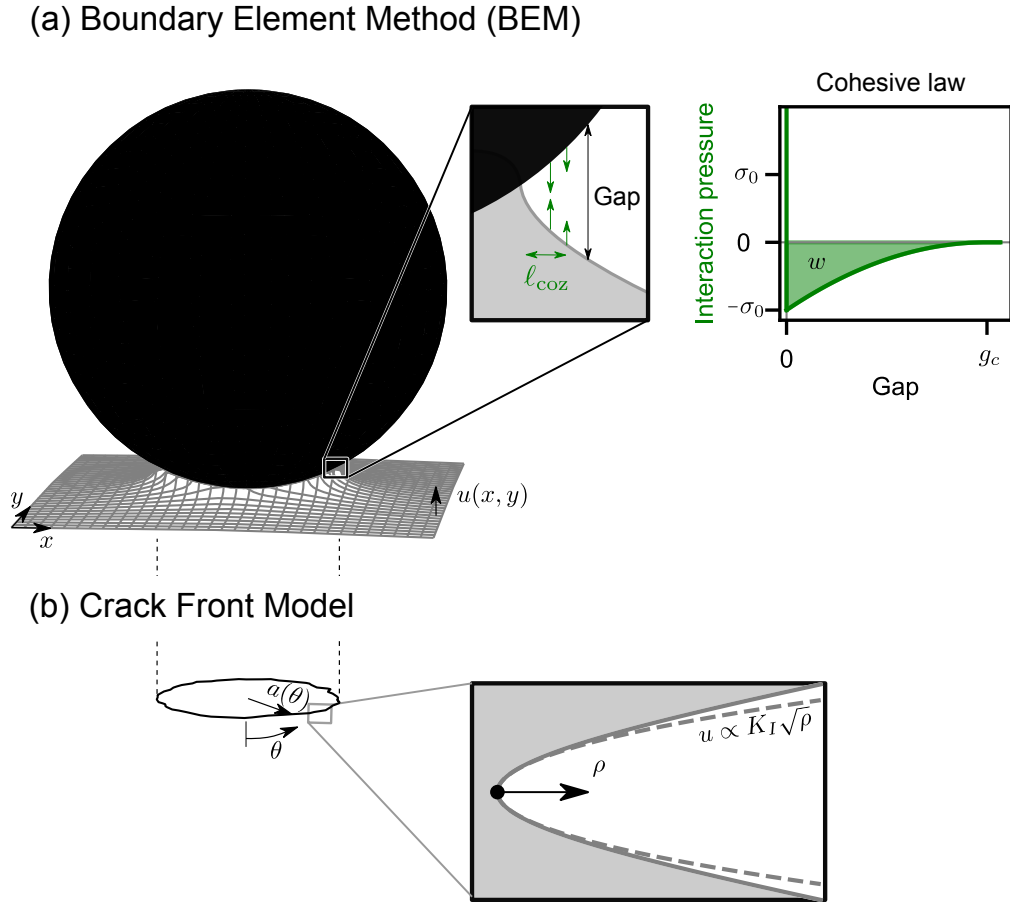


Figure 1: Schematic illustration of the two types of models used in this work to describe the contact of a sphere. (a) In the boundary element method (BEM), the surface displacements  $u(x, y)$  are computed using the Green's function of the elastic half-space and adhesive attractions are modeled using a cohesive law that relates the interaction pressure to the gap between the two surfaces. The integral over the cohesive law gives the work of adhesion  $w$ . Spatial heterogeneity is encoded into the cohesive law. (b) In the crack-front model, the state of the nearly circular contact is described by the contact radius as a function of angle  $a(\theta)$ . The heterogeneous work of adhesion distorts the shape of the crack front. The elastic response of the contact line is approximated using the first-order variation of the stress intensity factor with respect to the contact shape developed by Gao and Rice (1987a).

is the median work of adhesion. The equations are in dimensional form but can be nondimensionalized by substituting  $R = 1$ ,  $w_m = 1/\pi$  and  $E' = 3/4$ .

### 3. Reference model

We used the BEM to validate the crack-front models. BEM computes the surface displacements  $u(x, y)$  (Fig. 1a) minimizing the total energy  $\Pi$  at prescribed rigid body penetration  $\Delta$ . This method makes no assumptions on the contact morphology, allowing for holes and disconnected contact islands, but it is computationally too expensive to properly discretize contacts with small heterogeneities.

The mechanical energy  $\Pi_{\text{mech}} = U_{\text{el}}$  and its gradients are computed using the Green's function for pressures that are constant on each pixel (Love, 1929; Johnson, 1985). While the Green's function is nonperiodic, we accelerated calculations with a fast Fourier transform (Stanley and Kato, 1997; Campañá and Müser, 2006; Pastewka et al., 2012) by introducing a padding region that decouples periodic images (Hockney, 1970; Liu et al., 2000; Pastewka and Robbins, 2016).

The surface energy needs to be regularized using an interaction potential  $\phi$  between the surfaces (cohesive law),

$$\Pi_{\text{surf}} = \int_{-\infty}^{+\infty} dx dy \phi(w(x, y), g(x, y)), \quad (2)$$

where  $w(x, y)$  is the (spatially varying) work of adhesion and  $g(x, y)$  is the gap between the surfaces. The results converge to the JKR limit for small pixel size and interaction range, i.e. high Tabor parameter  $\mu_T$  (Muller et al., 1980; Maugis, 1992; Greenwood, 1997; Müser, 2014), but the point of instability where the two interfaces jump into contact converges particularly slowly with the interaction range (Wu, 2010; Ciavarella et al., 2017). Wang et al. (2021) could slightly retard the premature jump into contact by using a potential with a cutoff. Our choice of cohesive law,

$$\phi(w, g) = \begin{cases} -w \left(1 - \frac{g}{g_c}\right)^3, & g < g_c \\ 0, & \text{else} \end{cases}, \quad (3)$$

is based on the same observation. Equation (3) describes a cubic potential where  $w$  is the work of adhesion,  $g$  is the gap and  $g_c$  the cutoff distance. The derivative of  $\phi$  (interaction pressure) is illustrated in Fig. 1a. The maximum attractive stress  $\sigma_0 = 3w/g_c$  occurs at the perimeter of the contact area, where  $g = 0$ . To model (chemical) heterogeneity, the interaction parameters are different in each pixel. We keep  $g_c$  constant, so that  $\sigma_0$  and  $w$  vary proportionally from pixel to pixel.

The surfaces repel each other with a hard-wall potential, which is implemented as inequality constraints ( $g(x, y) \geq 0$ ) in the minimization algorithms. We used the constrained quasi-newton algorithm L-BFGS-B (Byrd et al., 1995) and a constrained conjugate gradient algorithm (Polonsky and Keer, 1999; Vollebregt, 2014; Bugnicourt et al., 2018) to minimize the energy. The latter algorithm is parallelized with the message passing interface and was used to produce precise reference solutions for the contact

shape, but could not be used in the presence of instabilities. Note that these minimization algorithms require that the interaction potential has a continuous second derivative, justifying our choice of a third-order polynomial. BEM with hard-wall repulsion and finite-ranged attraction (Müser, 2014, 2016; Müser et al., 2017; Wang and Müser, 2017; Bazrafshan et al., 2017; Rey et al., 2017; Bugnicourt et al., 2018; Monti et al., 2021) or soft (Lennard-Jones type) repulsion (Greenwood, 1997; Feng, 2000; Wu, 2010; Medina and Dini, 2014; Pastewka and Robbins, 2014, 2016; Persson and Scaraggi, 2014; Monti et al., 2019; Ghanbarzadeh et al., 2020; Wang et al., 2021) have been used in the past to study the adhesion of spheres and rough surfaces. During retraction, these models are similar to fiber-bundle models of quasi-brittle fracture (Batrouni et al., 2002; Schmittbuhl et al., 2003; Stormo et al., 2012; Gjerden et al., 2013, 2014) and threshold-force models (Pohrt and Popov, 2015; Hulikal et al., 2017; Li et al., 2019).

The finite interaction range introduces a cohesive zone around the contact perimeter in which the surfaces attract each other. This cohesive zone needs to be small in comparison to the scale of the heterogeneity (Chen et al., 2008) in order to mimic a JKR-like contact. We estimate the width of the cohesive zone using a Dugdale model and assume it is small in comparison to the contact radius (Maugis, 2010):

$$\ell_{\text{coz}} = \frac{\pi K_I^2}{8\sigma_0^2} = \frac{\pi E' w}{4\sigma_0^2} \quad (4)$$

For uniform work of adhesion, Müser (2014) showed that the (nondimensionalized) contact radius difference with the JKR limit is asymptotically  $\sim \ell_{\text{coz}}^* \sim \mu_T^{-2}$ , where  $\ell_{\text{coz}}^* = \ell_{\text{coz}} / (3\pi w_m R^2 / 4E')^{1/3}$  is the nondimensionalized cohesive zone width, see section 2. We use  $\ell_{\text{coz}}^*$  as a proxy for interaction range and Tabor parameter  $\mu_T$  (Tabor, 1977; Muller et al., 1980; Maugis, 1992). We chose the pixel size  $\ell_{\text{pix}}$  small enough so that further grid refinement affects the contact radius and the force less than decreasing the interaction range.

#### 4. Crack-front model

The crack-front model is a first-order perturbation from the axisymmetric JKR-contact of a sphere (Johnson et al., 1971; Barthel, 2008) using Rice’s weight function theory (Rice, 1985a; Gao and Rice, 1987a; Rice, 1989).

##### 4.1. Axisymmetric contact: The JKR model

We briefly review the JKR model of the adhesion of a sphere against an elastic half-space. JKR described the contact by the balance of elastic and surface energy of a circular crack (Griffith and Taylor, 1921). At equilibrium, the contact radius  $a$  is such that the increment of mechanical energy equals the increment of surface energy:

$$\frac{\partial \Pi_{\text{mech}}(a, \Delta)}{\partial a} = 2\pi a w(a) \quad (5)$$

$\Pi_{\text{mech}}$  is the mechanical potential and  $w$  is the work of adhesion at the perimeter of the contact. In this paper, we consider only boundary conditions with fixed rigid body penetration  $\Delta$ , where  $\Pi_{\text{mech}}$  is the elastic energy  $U_{\text{el}}$ .

The elastic energy release rate,

$$G(a, \Delta) = \frac{1}{2\pi a} \frac{\partial \Pi_{\text{mech}}(a, \Delta)}{\partial a}, \quad (6)$$

can be related to the intensity  $K$  of the singularity of the stress field near the crack tip (Irwin, 1957):

$$G = \frac{K^2}{2E'}. \quad (7)$$

JKR obtained the stress intensity factor  $K_J$  for sphere on flat contact by superposing contact pressures of the Hertzian sphere (Hertz, 1881) and of the circular flat punch (Sneddon, 1946; Maugis, 2010):

$$K_J(a, \Delta) = \left( \frac{a^2}{R} - \Delta \right) \frac{E'}{\sqrt{\pi a}} \quad (8)$$

Inserting Eqs. (6) to (8) into Eq. (5) yields an equilibrium equation for the contact radius as a function of the rigid body penetration. The normal force follows from the same superposition (Johnson et al., 1971; Maugis, 2010):

$$F_J(a, \Delta) = \frac{4E'}{3R} a^3 + 2aE' \left( \Delta - \frac{a^2}{R} \right) \quad (9)$$

The increment in surface energy is the integral of the work of adhesion within the area swept by the contact line. The JKR theory applies to any axisymmetric work of adhesion, where  $w$  depends on the radius in Eq. (5).

#### 4.2. Equilibrium condition for non-circular contacts

We now consider the perimeter of a nearly circular contact. The function  $a(s)$  represents the planar distance between the point at arc length  $s$  on the contact perimeter (or crack front) and the tip of the sphere. The mechanical potential is now a *functional* of the contact radius  $a$ . The elastic energy release rate  $G(s) = \delta \Pi_{\text{mech}} / \delta a(s)$  is the functional derivative of the mechanical potential  $\Pi_{\text{mech}}$  with respect to the contact radius:

$$\delta \Pi_{\text{mech}}([\delta a]) = \oint ds \delta a(s) G(s) \quad (10)$$

We omit the penetration  $\Delta$  and the contact shape  $a$  from the arguments for brevity. Note that  $ds \delta a(s)$  is an infinitesimal surface increment, so that  $G$  is an energy per surface area, as in Eq. (6). Here and below we use square brackets  $[\cdot]$  to indicate a functional dependence.

The stationarity of the total potential, i.e. the Griffith criterion, requires that the mechanical energy release rate at point  $s$  on the contact perimeter equals the local work of adhesion at the point  $(a(s), s)$  on the heterogeneous plane:

$$G(s) = w(a(s), s) \quad (11)$$

$G$  is available in closed form only for simple crack and contact shapes. Rice's weight function theory allows us to compute efficient approximations of  $G$  when perturbed from a reference configuration.

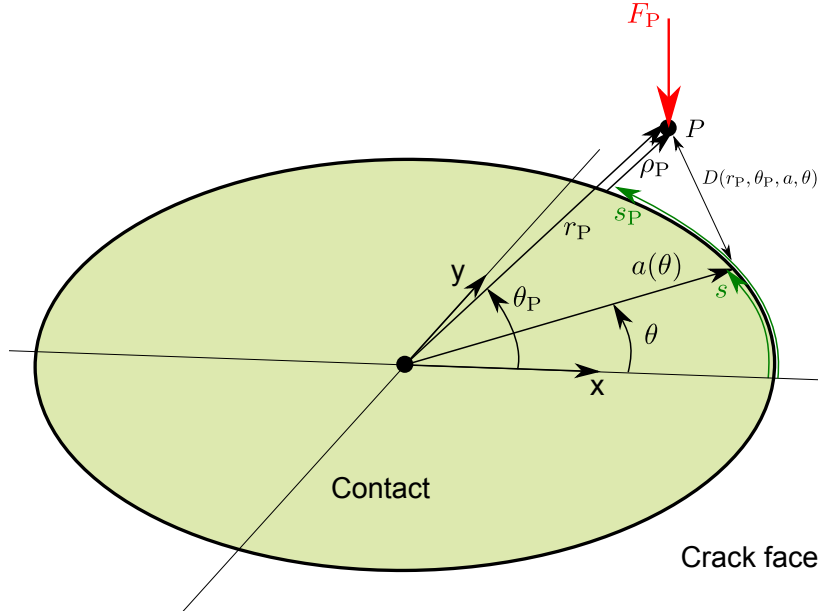


Figure 2: The crack-face weight function  $k$  is central in the derivation of the first-order variation of the stress intensity factor.  $k_J(a, r_P, \theta_P, \theta)$  corresponds to the stress intensity factor at angle  $\theta$  when a unit point force  $F_P$  is applied on the face of a circular external crack at  $r_P, \theta_P$ . The origin of the coordinate system is aligned with the tip of the spherical indenter.

Below we will parameterize the crack front using the angle  $\theta$  instead of the arc length  $s$ , see Fig. 2. In this new parameterization,

$$\delta\Pi_{\text{mech}}([\delta a]) = \oint ds G(s)\delta a(s) = \int_0^{2\pi} d\theta a(\theta)G(\theta)\delta a(\theta), \quad (12)$$

so that the functional derivative of the potential

$$\frac{\delta\Pi_{\text{mech}}}{\delta a(\theta)} = a(\theta)G(\theta) \quad (13)$$

instead of  $G(\theta)$ .

#### 4.3. First-order variation of the stress intensity factor

Rice showed that the sensitivity of the stress intensity factor to the contact shape  $\delta K/\delta a$  is linked to the crack-face weight function. The crack-face weight function  $k([a]; P, s)$  is the stress intensity factor caused by a unit force at point  $P$  outside the contact area and is known for simple geometries (Tada et al., 2000). While Rice's first variation of  $K$  was almost exclusively applied to flat-on-flat contact geometries (planar crack problems),  $\delta K/\delta a$  is unaffected by the presence of the Hertzian displacements in the contact area (Rice, 1985b; Borodachev, 1991). To make explicit that the first-order variation of  $K$



for circular connections (Gao and Rice, 1987a) applies also to the contact of spheres, we review the main steps leading to  $\delta K/\delta a$ .

We apply a force  $F_P$  on the elastic half-space at point  $P$  outside the contact area (on the crack face). This point force causes the displacement  $u_P$  at  $P$ . At fixed rigid body penetration  $\Delta$  and fixed force  $F_P$ , the mechanical potential is the Legendre transform of the elastic strain energy  $U_{\text{el}}$ ,

$$\Pi_{\text{mech}}(F_P) = \min_{u_P} \{U_{\text{el}}(u_P) - u_P F_P\}, \quad (14)$$

with derivatives

$$\left. \frac{\partial \Pi_{\text{mech}}}{\partial F_P} \right|_a = -u_P \quad \text{and} \quad \left. \frac{\delta \Pi_{\text{mech}}}{\delta a(s)} \right|_{F_P} = \left. \frac{\delta U_{\text{el}}}{\delta a(s)} \right|_{u_P} = G(s). \quad (15)$$

$U_{\text{el}}$  is the strain energy and  $-u_P F_P$  is the potential of the applied force  $F_P$ . Because the second derivatives of  $\Pi_{\text{mech}}$  are continuous, the order of differentiation does not matter (Schwartz's theorem):

$$\frac{\delta u_P}{\delta a(s)} = -\frac{\partial G(s)}{\partial F_P}. \quad (16)$$

From Eq. (7) and  $\partial K/\partial F_P = k([a]; P, s)$  we obtain

$$\frac{\delta u_P}{\delta a(s)} = -\frac{1}{E'} K(s) k([a]; P, s). \quad (17)$$

Setting  $F_P = 0$  (for arbitrary  $P$ ) we see that the crack-face weight function  $k$  describes how the crack faces deform when the crack front moves.

Knowing that the displacements near the crack tip correspond to the stress intensity factor, we can now deduce how the stress intensity factor is affected by a perturbation of the contact radius  $\delta a$ . At the perpendicular distance  $\rho_P$  away from the point  $s_P$  on the crack tip,

$$u(\rho_P, s_P) = \frac{4}{E'} \sqrt{\frac{\rho_P}{2\pi}} K(s_P) + \mathcal{O}(\rho_P^{3/2}). \quad (18)$$

From Eq. (18), the perturbation of the stress intensity factor becomes

$$\begin{aligned} \delta K(s_P) &= \lim_{\rho_P \rightarrow 0} \frac{E'}{4} \sqrt{\frac{2\pi}{\rho_P}} \oint ds \delta a(s) \frac{\delta u(\rho_P, s_P)}{\delta a(s)} \\ &= - \lim_{\rho_P \rightarrow 0} \sqrt{\frac{\pi}{8\rho_P}} \oint ds \delta a(s) K(s) k([a]; \rho_P, s_P, s), \end{aligned} \quad (19)$$

for  $\delta a$  restricted to  $\delta a(s_P) = 0$ . Rice introduced this restriction to ensure that  $\delta \rho_P = 0$ . As a consequence, Eq. (19) is not a first order variation because  $\delta a$  is not arbitrary. This restriction will be relaxed later by expanding the circular reference configuration by  $\delta a(s_P)$ .

When the contact perimeter is a circle ( $a(s) = \text{const.}$ ), we know  $K$  from Johnson et al. (1971) and  $k$  from Galin (Gladwell, 2008), enabling us to evaluate Eq. (19). For convenience, we now parameterize the position along the contact line with the angle  $\theta$  instead of the arc length  $s$ .

The crack-face weight function for the JKR contact is the same as for a circular connection. For a circular connection with radius  $a$  and fixed displacements at infinity (Gao and Rice, 1987a; Rice, 1989; Gladwell, 2008),

$$k_J(a, r_P, \theta_P, \theta) = \frac{\sqrt{(r_P^2 - a^2)/(a\pi^3)}}{D^2(r_P, \theta_P, a, \theta)}, \quad (20)$$

where  $D^2(r_P, \theta_P, a, \theta) = a^2 + r_P^2 - 2ar_P \cos(\theta_P - \theta)$  is the square of the distance between the point of application of the force on the crack face,  $P = (r_P, \theta_P)$ , and the point on the crack-front where the stress intensity factor is calculated,  $\theta$ . Note that  $k_J$  is not a functional of the whole radius, since in JKR the underlying contact area is a circle with radius  $a$ .

First applying a uniform perturbation of magnitude  $\delta a(\theta_P)$  to the circular reference contact (radius  $\tilde{a}_0$ ) and then using  $K = K_J$  and inserting Eq. (20) into Eq. (19) yields the first order variation of  $K(\theta_P)$  at  $a = \tilde{a}_0 = \text{const.}$ :

$$\delta K(\theta_P) = \frac{\partial K_J(\tilde{a}_0)}{\partial \tilde{a}_0} \delta a(\theta_P) - \frac{K_J(\tilde{a}_0)}{8\pi} \text{PV} \int_0^{2\pi} d\theta \frac{\tilde{a}_0(\delta a(\theta) - \delta a(\theta_P))}{D^2(r_P, \theta_P, \tilde{a}_0, \theta)} \quad (21)$$

We point to Gao and Rice (1987a,b) for details on how the limit  $\rho_P \rightarrow 0$  leads to the Cauchy principal value integral PV  $\int$ .

We now recast Eq. (21) using the Fourier series of  $a$ . Inserting

$$a(\theta) = \sum_{n \in \mathbb{Z}} \tilde{a}_n e^{in\theta} \quad (22)$$

into Eq. (21) yields

$$\delta K(\theta_P) = \frac{\partial K_J(\tilde{a}_0)}{\partial \tilde{a}_0} \delta a(\theta_P) + \frac{K_J(\tilde{a}_0)}{\tilde{a}_0} \sum_{n \in \mathbb{Z} \setminus \{0\}} \frac{|n|}{2} \delta \tilde{a}_n e^{in\theta_P}. \quad (23)$$

From the inverse of Eq. (22),

$$\tilde{a}_n = \frac{1}{2\pi} \int_0^{2\pi} d\theta e^{-in\theta} a(\theta), \quad (24)$$

we obtain  $\delta \tilde{a}_n / \delta a(\theta) = \exp(-in\theta) / 2\pi$ . The functional derivative of  $K$  then becomes

$$\frac{\delta K}{\delta a(\theta)} = \frac{\partial K_J(\tilde{a}_0)}{\partial \tilde{a}_0} \delta(\theta - \theta_P) + \frac{K_J(\tilde{a}_0)}{2\pi \tilde{a}_0} \sum_{n \in \mathbb{N}} |n| \cos n(\theta_P - \theta), \quad (25)$$

which depends only on  $|\theta - \theta_P|$ . The translational invariance reflects the axial symmetry of the unperturbed state. As will be discussed in a few paragraphs,  $\theta$  and  $\theta_P$  commute because  $\delta K / \delta a(\theta)$  is related to the second derivative of the energy.

The key step leading to  $\delta K / \delta a(\theta)$  was recognizing the symmetry of the derivatives of the elastic energy, Eq. (16), that follows from the smoothness of the elastic energy. Hence, Eq. (25) not only applies to flat indenters (Rice, 1985a; Gao and Rice, 1987a,b; Rice, 1989), but also to contacts against spheres or any smooth indenters. All the relevant information of the axisymmetric contact geometry is in  $K_J$  and its derivatives. Knowing the first order variation of  $K$  when the contact is perfectly circular allows us to approximate the equilibrium Eq. (11) to first order in the perturbation from circularity.

#### 4.4. Quadratic approximation of the deformation energy

The straightforward approach to construct a first order model is to linearly extrapolate either  $G$  or  $K$ . However, these approximations do not conserve the variational property of  $aG$ , i.e. that it is the gradient of a potential, Eq. (13). We now guess a quadratic approximation for the elastic energy and verify a posteriori that it possesses the exact first and second derivatives at  $a(\theta) = \tilde{a}_0$ . Our guess for the elastic energy is

$$U_{\text{el}} = \frac{1}{2\pi} \int_0^{2\pi} d\theta U_{\text{J}}(a(\theta)) + \pi G_{\text{J}}(\tilde{a}_0) \sum_n |n| |\tilde{a}_n|^2 \quad (26)$$

with first derivative

$$\frac{\delta U_{\text{el}}}{\delta a(\theta)} = \frac{1}{2\pi} \frac{\partial U_{\text{J}}(a(\theta))}{\partial a(\theta)} + G_{\text{J}}(\tilde{a}_0) \sum_n |n| \tilde{a}_n e^{in\theta} + \frac{1}{2} \frac{\partial G_{\text{J}}(\tilde{a}_0)}{\partial \tilde{a}_0} \sum_n |n| |\tilde{a}_n|^2 \quad (27)$$

and second derivative

$$\begin{aligned} \frac{\delta^2 U_{\text{el}}}{\delta a(\theta) \delta a(\theta_{\text{P}})} &= \frac{1}{2\pi} \frac{\partial^2 U_{\text{J}}(a(\theta))}{\partial a^2(\theta)} \delta(\theta - \theta_{\text{P}}) + \frac{1}{2\pi} G_{\text{J}}(\tilde{a}_0) \sum_n |n| e^{in(\theta - \theta_{\text{P}})} \\ &+ \frac{1}{2\pi} \frac{\partial G_{\text{J}}(\tilde{a}_0)}{\partial \tilde{a}_0} \sum_n |n| \tilde{a}_n (e^{in\theta} + e^{in\theta_{\text{P}}}) + \frac{1}{4\pi} \frac{\partial^2 G_{\text{J}}(\tilde{a}_0)}{\partial \tilde{a}_0^2} \sum_n |n| |\tilde{a}_n|^2. \end{aligned} \quad (28)$$

$U_{\text{J}}$  is the elastic energy in the perfectly circular contact (Johnson et al., 1971) and  $\partial U_{\text{J}}/\partial a = 2\pi a G_{\text{J}}(a)$ . It is straightforward to show that Eq. (28) for  $a(\theta) = \tilde{a}_0$  gives Eq. (25). We determine the contact shape by solving (see also Eq. (13))

$$\frac{\delta U_{\text{el}}}{\delta a(\theta)} - w(\theta, a(\theta))a(\theta) = 0 \quad (29)$$

using a minimization algorithm (see section 4.7). We will call this model CF-E when presenting our results.

The normal force applied on the indenter follows directly from our approximation of the energy:

$$F = \frac{\partial U_{\text{el}}(\Delta, a)}{\partial \Delta}. \quad (30)$$

Using Eq. (26),

$$F(a, \Delta) = \frac{1}{2\pi} \int_0^{2\pi} d\theta F_{\text{J}}(a(\theta), \Delta) + \pi \frac{\partial G_{\text{J}}(\tilde{a}_0, \Delta)}{\partial \Delta} \sum_n |n| |\tilde{a}_n|^2. \quad (31)$$

#### 4.5. Other first order approximations

As a benchmark we also consider two common first order approximations of the crack front. The first approximation linearly extrapolates the stress intensity factor and solves for  $K = K_{\text{c}} = \sqrt{2E'w}$  (Gao and Rice, 1989; Fares, 1989):

$$K(\theta) = K_{\text{J}}(\tilde{a}_0) + \frac{\partial K_{\text{J}}(\tilde{a}_0)}{\partial \tilde{a}_0} (a(\theta) - \tilde{a}_0) + \frac{K_{\text{J}}(\tilde{a}_0)}{\tilde{a}_0} \sum_{n \in \mathbf{Z}} \frac{|n|}{2} \tilde{a}_n e^{in\theta}. \quad (32)$$

We will refer to this model as CF-K.

The second approximation linearly extrapolates the energy release rate and solves for  $G = w$  (Bonamy et al., 2008; Chopin et al., 2015; Ponsou, 2016):

$$G(\theta) = G_J(\tilde{a}_0) + \frac{\partial G_J(\tilde{a}_0)}{\partial \tilde{a}_0}(a(\theta) - \tilde{a}_0) + \frac{G_J(\tilde{a}_0)}{\tilde{a}_0} \sum_{n \in \mathbf{Z}} |n| e^{in\theta} \tilde{a}_n. \quad (33)$$

We will refer to this model as CF-G.

An alternative first order extrapolation,

$$G(\theta) = G_J(a(\theta)) \left( 1 + \frac{1}{a(\theta)} \sum_{n \in \mathbf{Z}} |n| e^{in\theta} \tilde{a}_n \right),$$

should in principle be more accurate, because  $G_J(a(\theta))$  is not linearized. However we observed that using the latter equation does not improve the prediction of the normal force and Eq. (33) is better suited for analytical models. We did the same observation with the analogous expression for the stress intensity factor.

Because these crack-front models do not possess an elastic energy, we cannot use Eq. (30) to compute the normal force. As an approximation, we neglect the effect of the undulations of the crack front on the normal force and insert the mean contact radius  $\tilde{a}_0$  into the expression for a perfectly circular contact, Eq. (9). We will discuss in section 5 that the crack shape affects the normal force only to second order.

#### 4.6. Symmetries

Rice obtained the first order variation of  $K$  (Eq. (25)) from the symmetry of second derivatives (or the path independence of the work) with respect to the contact radius and a point force applied on the crack face. Similarly, the second derivatives with respect to the contact radius are symmetric (Gao and Rice, 1989; Leblond et al., 2012; Salvadori and Fantoni, 2014):

$$\frac{\delta^2 U}{\delta a(\theta) \delta a(\theta_P)} = \frac{\delta^2 U}{\delta a(\theta_P) \delta a(\theta)} \quad (34)$$

For the energy release rate, it follows from Eq. (13) that  $a(\theta) \delta G(\theta) / \delta a(\theta_P)$  should be symmetric.

The linear extrapolation of  $K$  (Eq. (32)) violates this symmetry. Linearizing  $G$  (Eq. (33)) fulfills the symmetry only for translational invariance in the crack propagation direction,  $\partial G_J / \partial a = 0$ , i.e. in the case of a semi-infinite crack (Leblond et al., 2012).

#### 4.7. Numerical implementation of the crack-front model

For a fixed penetration  $\Delta$ , we solve for the equilibrium of energy release rate and work of adhesion in  $N$  collocation points at evenly spaced angles  $\theta_j$  (Eq. (11)). This turns the functional derivatives presented above into partial derivatives and  $\tilde{a}_n$  becomes the discrete Fourier transform of the contact radius. To discretize integrals like  $\int_0^{2\pi} d\theta U_J(a(\theta))$ , we take  $a$  constant on each angle element of size  $\Delta\theta = 2\pi/N$ .

We are interested in stable equilibria, therefore it is important to use a minimization algorithm and not a root finder. When we simulate the indentation and retraction

process, we use the solution obtained at the previous penetration as initial guess. This procedure mimics the quasi-static dynamics of the contact, where the crack front moves to the closest metastable state.

When the crack front moves to the next metastable state through an instability, we need a robust minimization algorithm. We use a trust-region Newton conjugate-gradient algorithm (Steihaug, 1983; Nocedal and Wright, 2006, Algorithm 7.2), where we *fix* the radius of the trust region. Since the work of adhesion field is the source of nonlinearity, the trust radius needs to be slightly smaller than the size of the heterogeneity. If the minimum contact radius is smaller than this value during a Newton step, the trust region is further reduced below the contact radius in order to avoid negative contact radii. Note that trust-region algorithms usually tune the radius according to the discrepancy between the quadratic subproblem and the actual potential. We omitted that feature because, as discussed above, some crack-front models do not possess an elastic energy. An alternative to fixing the trust radius would be to tune it according to gradients instead of energies.

## 5. Validation and comparison of the perturbation methods

We investigate which first-order crack-perturbation method – linear extrapolation of  $K$  (CF-K, Eq. (32)), linear extrapolation of  $G$  (CF-G, Eq. (33)) or quadratic extrapolation of the energy (CF-E, Eqs. (26)-(28)) – describes most accurately the contact area and the normal force. We use BEM simulations with  $\ell_{\text{coz}}^* \simeq 0.0007$  and pixel size  $\ell_{\text{pix}}^* = 0.00015625$  as a reference, the grid size is  $32768 \times 32768$  without the padding region. As a test case, we consider the ray-shaped work of adhesion heterogeneity (see inset to Fig. 3a)

$$w(r, \theta) = w_m + \Delta w \cos(n_{\text{rays}} \theta), \quad (35)$$

where we vary  $n_{\text{rays}}$  and  $\Delta w$ . We fix the value of the penetration to  $\Delta^* = 1$ .

Figure 3a,b compares the contact geometry obtained from BEM and the different crack-front models for  $\Delta w = 0.4$  and 4 rays (Fig. 3a) and 64 rays (Fig. 3b). To estimate the remaining deviations of BEM from the short-ranged limit, we also show a BEM simulation with a four times larger cohesive zone ( $\ell_{\text{coz}}^* \simeq 0.0028$ ) and pixel size ( $\ell_{\text{pix}}^* = 0.000625$ ,  $8192 \times 8192$  pixels). For decreasing  $\ell_{\text{coz}}^*$ , the contact radius increases and the normal force decreases and when the work of adhesion is uniform, the normal force converges towards the JKR solution (Fig. 3c) This convergence behavior is consistent with reports in Maugis (1992), Greenwood (1997) and Müser (2014).

For  $n_{\text{rays}} = 4$  (Fig. 3a), the contact shapes of all crack-front models are similarly close to the BEM results. While CF-K fits better in the peak and the valley of the undulation, CF-G and CF-E are closer to BEM between these two locations. For  $n_{\text{rays}} = 64$  (Fig. 3b), the crack-front models differ more clearly but the errors due to the finite interaction range in BEM are also relatively large. However, as we mentioned in the previous paragraph, the short-ranged limit has slightly higher contact radii than our reference simulation. Therefore we conclude that for large  $n_{\text{rays}}$ , the contact radius is significantly underestimated by CF-K.

The crack-front models unambiguously differ in the prediction of the normal force. The CF-E model best captures how the normal force depends on the heterogeneity wavelength (Fig. 3c) and amplitude (Fig. 3d). The deviations of CF-G from CF-E are small and disappear for small heterogeneities. CL-K has the largest discrepancies and predicts

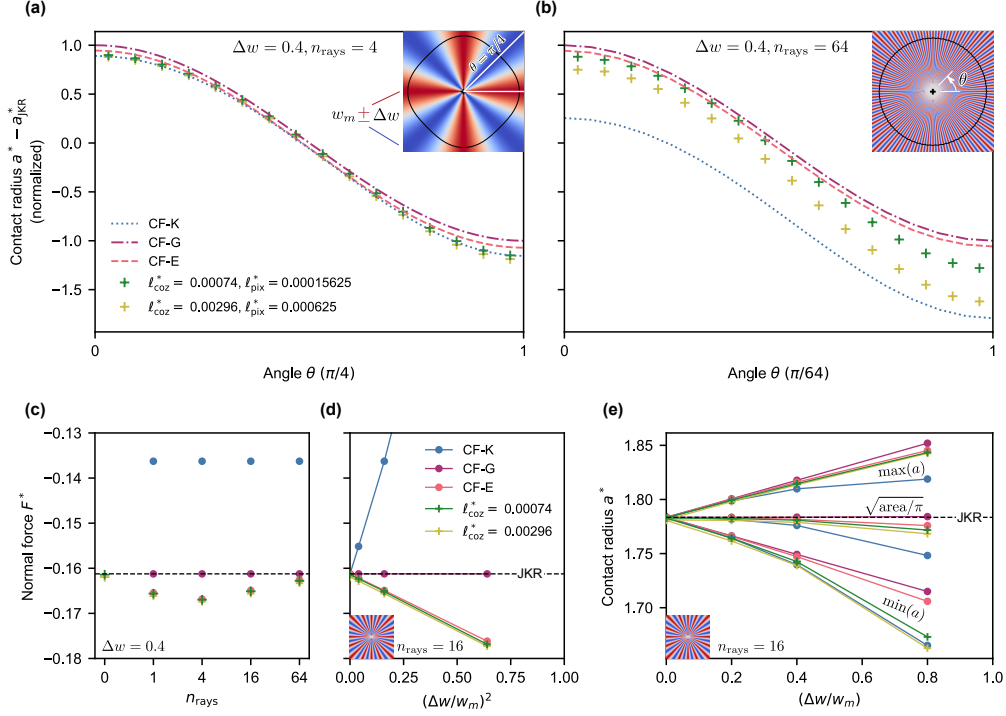


Figure 3: Comparison of the different crack-front models with BEM simulations for ray-shaped work of adhesion heterogeneity. (a,b) Contact radii computed using BEM and the different CF models on the cosinusoidal work of adhesion landscapes illustrated in the insets. We show the contact radii  $a(\theta)$  only over a half period of heterogeneity. We used the radii predicted by CF-G (Eq. (33)) to normalize the contact radius. Since the amplitude of the contact radius is roughly proportional to the wavelength of the heterogeneity, the magnification is higher for  $n_{\text{rays}} = 64$  and the effect of the cohesive zone size in the BEM simulations is more apparent. (c) Normal force as a function of the number of rays.  $n_{\text{rays}} = 0$  corresponds to a uniform work of adhesion, where it can be verified that BEM is close to the short-range limit (JKR).  $F^*$  is the normal force normalized by  $\pi w_m R$ , as discussed in section 2. (d) Normal force as a function of the (squared) amplitude of the work of adhesion heterogeneity, for  $n_{\text{rays}} = 16$ . In the crack-front models CF-K and CF-G, the normal force is computed by inserting the mean contact radius into the JKR equation (Eq. (9)). In CF-E, the normal force is computed by taking the derivative of the elastic energy (Eq. (31)). (e) Contact area, minimum contact radius and maximum contact radius in BEM simulations and different crack-front models as a function of the amplitude of the work of adhesion heterogeneity.

less adhesive normal forces. However, all errors are relatively small because the leading order contribution of  $\Delta w$  to the normal forces is of second order in BEM and in all the crack-front models. This scaling has been pointed out by Argatov (2021) and is visible in Fig. 3d, where we represent the normal force as a function of  $\Delta w^2$ .

We now discuss qualitatively how the crack shapes depend on  $\Delta w$  (Fig. 3e). In all crack-front models, the amplitude of the contact radius undulation is smaller than in BEM. This is consistent with the numerical simulations of Fares (1989) and the second order perturbation by Leblond et al. (2012). As in Fares' simulations, the relation between contact radius and work of adhesion (i.e. stress intensity factor) is more nonlinear for the minimum contact radius than for the maximum contact radius.

Leblond et al. (2012) pointed out that for a semi-infinite crack ( $n_{\text{rays}} \rightarrow \infty$ ), the mean contact radius depends only on the mean work of adhesion along the crack front. Leblond's statement follows from the existence of an elastic potential and hence is satisfied by construction in CF-E. In CF-G (Eq. (33)), the mean contact radius  $\tilde{a}_0$  is independent of  $\Delta w$  at any  $n_{\text{rays}}$ ; in fact, CF-E and CF-G are identical in the limit  $n_{\text{rays}} \rightarrow \infty$ . CF-G conserves energy only in that limit. In contrast, in the CF-K model (Eq. (32)),  $\tilde{a}_0$  decreases with increasing  $\Delta w$ . The reason is that  $\tilde{a}_0$  depends only on the average fracture toughness: taking the average of Eq. (32) yields  $\langle K_c \rangle = K_J(\tilde{a}_0)$ . At fixed  $w_m$ ,  $\langle K_c \rangle \propto \langle \sqrt{w} \rangle$  decreases with increasing heterogeneity. This contact radius offset is independent of  $n_{\text{rays}}$  and becomes large compared to the undulation when  $n_{\text{rays}}$  increases (Fig. 3b). Therefore, by predicting too small contact radii, CF-K violates energy conservation. In summary, for large  $n_{\text{rays}}$ , the contact area is more accurate in CF-G and CF-E than in CF-K. Because CF-K underestimates the contact area, it also predicts less adhesive normal forces.

The main benefit of CF-E is that it allows us to define rigorously the normal force by Eq. (30). Inserting the Taylor expansion of  $F_J$  into Eq. (31), only terms of second order in the amplitude of the contact radius remain<sup>1</sup>.  $\partial^2 F_J / \partial a^2$  and  $\partial G_J / \partial \Delta$  are both negative, so that small-scale fluctuations of the contact radius lead to a more negative (more adhesive) force. Hence, fluctuations of the work of adhesion along the contact line slightly increase adhesion, which is in agreement with the BEM results in Fig. 3d. However, this effect vanishes for small heterogeneities (Fig. 3c): for large  $n$ ,  $\tilde{a}_n \propto \Delta w / n$ , so that  $F(a) - F_J(\tilde{a}_0) \propto \sum_n |n| |\tilde{a}_n|^2 \rightarrow 0$ .

To conclude, while all the crack-perturbation methods are valid first order approximations, the ansatz possessing an elastic energy (CF-E) yields the best overall results. At large  $n_{\text{rays}}$  (small heterogeneities), the CF-G model and the CF-E model are equivalent. The CF-G equation is simpler and can be used in analytical theories for crack pinning (Démery et al., 2014). For an amplitude of the heterogeneity of  $\Delta w \leq 0.4$ , the errors due to the finite interaction range in expensive BEM simulations are comparable to the errors of the first order perturbation models.

## 6. Application to a random heterogeneity

To illustrate the usefulness of the crack-front model to study the adhesion hysteresis, we simulated the indentation and retraction of a sphere with randomly fluctuating work

---

<sup>1</sup>The first term in the Taylor expansion of  $F_J$  around  $a(\theta) = \tilde{a}_0$  disappears by averaging over the perimeter.

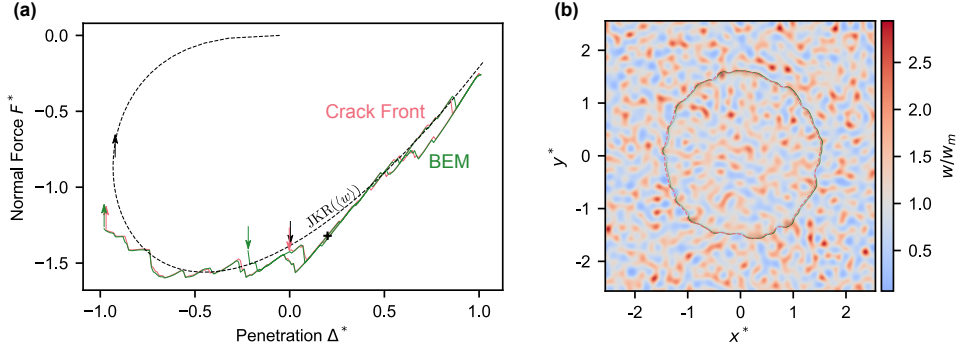


Figure 4: (a) Force-penetration curves from a boundary element method (BEM) and a crack-front simulation (CF-E) on the spatially random work of adhesion shown in panel (b). We also show the prediction by the JKR model for a homogeneous surface at the same average work of adhesion. The arrows indicate the jump into contact and the jump out of contact instabilities. (b) Contact areas at the penetration  $\Delta^* = 0.2$ , indicated by the cross in the force-penetration curve, on top of the work of adhesion field. The tensile pressures of the contact mechanics simulation are shown in green, so that the perimeter of the contact is indicated by the darkest green pixels. The pink dashed line is the contact perimeter calculated with the crack-front model. The work of adhesion field has a standard deviation  $\simeq 0.4w_m$  and a short wavelength cutoff at  $\ell_{\text{het}}^* = 0.2$ . We used the median work of adhesion  $w_m = \langle K_c \rangle^2 / 2E'$  for nondimensionalization.

of adhesion. We compare the results of BEM and the CF-E model in Fig. 4. The crack-front simulation yields almost the same result as BEM, but requires only one minute instead of one day of computational time. (Both simulations were performed on a single core.)

The BEM simulation was discretized on a  $1024 \times 1024$  grid with pixel size  $\ell_{\text{pix}}^* = 0.005$ . On the same grid, we generated a random Gaussian toughness field with mean  $\langle K_c \rangle = \sqrt{2E'w_m}$  and standard deviation  $K_{c,\text{rms}} = 0.2 \langle K_c \rangle$  (Fig. 4b). We chose a Gaussian fracture toughness field instead of a work of adhesion field because it is easier to avoid negative work of adhesion values. Because the work of adhesion is the square of a Gaussian field, the mean  $\langle w \rangle$  exceeds the median  $w_m$  by a factor 1.04. The standard deviation  $w_{\text{rms}} \simeq 0.39w_m$ . The Fourier spectrum is flat at wavelengths above the correlation length  $\ell_{\text{het}}^* = 0.2$  and 0 below. The interaction range corresponds to a cohesive zone size  $\ell_{\text{coz}}^* \simeq 0.012$ .

We performed a crack-front simulation on the same work of adhesion field. In order to evaluate the equilibrium condition of the crack front (Eq. (29)), we interpolated the work of adhesion with bicubic splines between the grid points. We used 512 collocation points on the crack front so that the largest spacing between the collocation points (at the maximal penetration) is  $\simeq \ell_{\text{het}}^*/10$ .

In both simulations, we increased the penetration  $\Delta^*$  in steps of 0.01 until the maximum penetration  $\Delta_{\text{max}}^* = 1$  was reached and then decreased it until pull off. The starting penetration was chosen to be lower than the jump into contact instability.

In Fig. 4a, the force-penetration curves computed with BEM and the crack-front model nearly overlap. For reference, we also show the force-penetration curve resulting



from a homogeneous work of adhesion (JKR model) having the same mean value. The homogeneous contact has one hysteresis loop corresponding to the jump into and the jump out of contact instabilities; the force is reversible at positive penetrations. In our simulations, the heterogeneities are energy barriers that pin the crack front and alter the normal force. The kinks in the force curve correspond to depinning instabilities that dissipate energy and lead to additional hysteresis loops (Joanny and de Gennes, 1984). The adhesion hysteresis caused by crack-front pinning will be discussed in more detail in an upcoming publication.

We now discuss the differences between the crack front and BEM results. In BEM, the jump into contact instability occurs too early: it converges much slower with interaction range than other quantities (Wu, 2010; Ciavarella et al., 2017; Wang et al., 2021). The remainder of the force-penetration curve, including depinning instabilities, is well converged. Other discrepancies in the force-penetration curves are due to the linearization in the crack-front model. The contact perimeters agree well, with the most significant deviations in the regions with low work of adhesion. This is consistent with what we observed in the previous section. The two simulations deviate more significantly at a few penetration values, where the instabilities occur at slightly different penetrations. An animation comparing the contact shape of BEM and the contact line during the whole indentation retraction process is provided in the supplementary material.

As mentioned at the beginning of this section, the crack-front simulations are computationally much cheaper than the BEM simulations. Furthermore, in BEM and in the crack-front model, the number of pixels in the linear dimension  $n$  scales with  $\ell_{\text{het}}^{-1}$  (the total number of pixels in BEM is then  $\sim n^2$ ). While in BEM, the computation time of the elastic deformations increases as  $n^2 \log n$  (two dimensional fast Fourier transform), in the crack-front model it only increases as  $n \log n$  (one dimensional fast Fourier transform). The crack-front model will enable us to simulate smaller heterogeneities and softer spheres than possible with traditional BEM approaches.

## 7. Conclusion

We described the adhesion of a sphere against a chemically heterogeneous surface by first-order crack perturbation and validated this model against a boundary element method (BEM). We compared different variants of the first-order perturbation and found that the best approach is to approximate the energy quadratically. Linearizing the energy release rate is equivalent in the limit of small heterogeneity size, but linearizing the stress intensity factor underestimates adhesion in that limit.

By its efficiency, the crack-front model allows us to simulate orders of magnitude larger systems than possible with BEMs. This simplified model requires, however, that the work of adhesion heterogeneity is sufficiently small for the contact area to be nearly circular. Adapting the crack-front model to surface roughness will allow us to test whether crack-front pinning can explain the role of surface roughness in adhesion hysteresis (Dalvi et al., 2019) and to make theoretical predictions based on previous work on pinning of elastic lines by a random field (Démery et al., 2014).

## Acknowledgments

We thank W. Beck Andrews, Ali Dhinojwala, Patrick Dondl, Andreas Greiner and Tevis D. B. Jacobs for useful discussion. We thank Sindhu Singh for implementing the constrained conjugate-gradients algorithm and Laura Mahoney for writing assistance. We are indebted to Mark O. Robbins for pointing us to the analogy to an elastic line. Funding was provided by the Deutsche Forschungsgemeinschaft (DFG, German Research Foundation) under Germany's Excellence Strategy – EXC-2193/1 – 390951807 and by the European Research Council (StG-757343). Numerical simulations were performed on bwForCluster NEMO (University of Freiburg, DFG grant INST 39/963-1 FUGG).

## References

- Amaral, L.A.N., Barabasi, A.L., Makse, H.A., Stanley, H.E., 1995. Scaling properties of driven interfaces in disordered media. *Phys. Rev. E* 52, 4087. doi:10.1103/PhysRevE.52.4087.
- Argatov, I.I., 2021. Controlling the adhesive pull-off force via the change of contact geometry. *Philos. Trans. R. Soc. London, Ser. A* 379, 20200392. doi:10.1098/rsta.2020.0392.
- Barthel, E., 2008. Adhesive elastic contacts: JKR and more. *J. Phys. D: Appl. Phys.* 41, 163001. doi:10.1088/0022-3727/41/16/163001.
- Batrouni, G.G., Hansen, A., Schmittbuhl, J., 2002. Heterogeneous interfacial failure between two elastic blocks. *Phys. Rev. E* 65, 036126. doi:10.1103/PhysRevE.65.036126.
- Bazrafshan, M., de Rooij, M.B., Valefi, M., Schipper, D.J., 2017. Numerical method for the adhesive normal contact analysis based on a Dugdale approximation. *Tribol. Int.* 112, 117–128. doi:10.1016/j.triboint.2017.04.001.
- Bonamy, D., Santucci, S., Ponson, L., 2008. Crackling dynamics in material failure as the signature of a self-organized dynamic phase transition. *Phys. Rev. Lett.* 101, 045501. doi:10.1103/PhysRevLett.101.045501.
- Borodachev, N.M., 1991. Contact problem for an elastic half-space with a near-circular contact area. *Soviet Appl. Mech.* 27, 118–123. doi:10.1007/BF00887799.
- Briggs, G.A.D., Briscoe, B.J., 1977. The effect of surface topography on the adhesion of elastic solids. *J. Phys. D: Appl. Phys.* 10, 2453–2466. doi:10.1088/0022-3727/10/18/010.
- Bugnicourt, R., Sainsot, P., Dureisseix, D., Gauthier, C., Lubrecht, A.A., 2018. FFT-based methods for solving a rough adhesive contact: Description and convergence study. *Tribol. Lett.* 66, 29. doi:10.1007/s11249-017-0980-z.
- Byrd, R.H., Lu, P., Nocedal, J., Zhu, C., 1995. A limited memory algorithm for bound constrained optimization. *SIAM J. Sci. Comput.* 16, 1190–1208. doi:10.1137/0916069.
- Campaña, C., Müser, M.H., 2006. Practical Green's function approach to the simulation of elastic semi-infinite solids. *Phys. Rev. B* 74, 075420. doi:10.1103/PhysRevB.74.075420.
- Carbone, G., Pierro, E., Recchia, G., 2015. Loading-unloading hysteresis loop of randomly rough adhesive contacts. *Phys. Rev. E* 92, 062404. doi:10.1103/PhysRevE.92.062404.
- Chen, B., Shi, X., Gao, H., 2008. Apparent fracture/adhesion energy of interfaces with periodic cohesive interactions. *Proc. R. Soc. London, Ser. A* 464, 657–671. doi:10.1098/rspa.2007.0240.
- Chen, Y.L., Helm, C.A., Israelachvili, J.N., 1991. Molecular mechanisms associated with adhesion and contact angle hysteresis of monolayer surfaces. *J. Phys. Chem.* 95, 10736–10747. doi:10.1021/j100179a041.
- Chopin, J., Boudaoud, A., Adda-Bedia, M., 2015. Morphology and dynamics of a crack front propagating in a model disordered material. *J. Mech. Phys. Solids* 74, 38–48. doi:10.1016/j.jmps.2014.10.001.
- Ciavarella, M., Greenwood, J.A., Barber, J.R., 2017. Effect of Tabor parameter on hysteresis losses during adhesive contact. *J. Mech. Phys. Solids* 98, 236–244. doi:10.1016/j.jmps.2016.10.005.
- Dalvi, S., Gujrati, A., Khanal, S.R., Pastewka, L., Dhinojwala, A., Jacobs, T.D.B., 2019. Linking energy loss in soft adhesion to surface roughness. *Proc. Natl. Acad. Sci. U.S.A.* 116, 25484–25490. doi:10.1073/pnas.1913126116.
- Dapp, W.B., Müser, M.H., 2015. Contact mechanics of and Reynolds flow through saddle points: On the coalescence of contact patches and the leakage rate through near-critical constrictions. *Europhys. Lett.* 109, 44001. doi:10.1209/0295-5075/109/44001.

- Démery, V., Rosso, A., Ponsou, L., 2014. From microstructural features to effective toughness in disordered brittle solids. *Europhys. Lett.* 105, 34003. doi:10.1209/0295-5075/105/34003.
- Deng, W., Kesari, H., 2017. Molecular statics study of depth-dependent hysteresis in nano-scale adhesive elastic contacts. *Modell. Simul. Mater. Sci. Eng.* 25, 055002. doi:10.1088/1361-651X/aa6ef8.
- Deng, W., Kesari, H., 2019. Depth-dependent hysteresis in adhesive elastic contacts at large surface roughness. *Sci. Rep.* 9, 1639. doi:10.1038/s41598-018-38212-z.
- Fares, N., 1989. Crack fronts trapped by arrays of obstacles: Numerical solutions based on surface integral representation. *J. Appl. Mech.* 56, 837–843. doi:10.1115/1.3176179.
- Feng, J.Q., 2000. Contact behavior of spherical elastic particles: A computational study of particle adhesion and deformations. *Colloids Surf., A* 172, 175–198. doi:10.1016/S0927-7757(00)00580-X.
- Fisher, D.S., 1983. Threshold behavior of charge-density waves pinned by impurities. *Phys. Rev. Lett.* 50, 1486–1489. doi:10.1103/PhysRevLett.50.1486.
- Fuller, K.N.G., Tabor, D., 1975. The effect of surface roughness on the adhesion of elastic solids. *Proc. R. Soc. London, Ser. A* 345, 327–342. doi:10.1098/rspa.1975.0138.
- Gao, H., Rice, J.R., 1987a. Nearly circular connections of elastic half spaces. *J. Appl. Mech.* 54, 627–634. doi:10.1115/1.3173080.
- Gao, H., Rice, J.R., 1987b. Somewhat circular tensile cracks. *Int. Journal of Fract.* 33, 155–174. doi:10.1007/BF00013168.
- Gao, H., Rice, J.R., 1989. A first-order perturbation analysis of crack trapping by arrays of obstacles. *J. Appl. Mech.* 56, 828–836. doi:10.1115/1.3176178.
- Ghanbarzadeh, A., Faraji, M., Neville, A., 2020. Deterministic normal contact of rough surfaces with adhesion using a surface integral method. *Proc. R. Soc. London, Ser. A* 476, 20200281. doi:10.1098/rspa.2020.0281.
- Gjerden, K.S., Stormo, A., Hansen, A., 2013. Universality classes in constrained crack growth. *Phys. Rev. Lett.* 111, 135502. doi:10.1103/PhysRevLett.111.135502.
- Gjerden, K.S., Stormo, A., Hansen, A., 2014. Local dynamics of a randomly pinned crack front: A numerical study. *Front. Phys.* 2, 66. doi:10.3389/fphy.2014.00066.
- Gladwell, G.M.L. (Ed.), 2008. *Contact Problems*. volume 155 of *Solid Mechanics and Its Applications*. Springer Netherlands, Dordrecht. doi:10.1007/978-1-4020-9043-1.
- Greenwood, J.A., 1997. Adhesion of elastic spheres. *Proc. R. Soc. London, Ser. A* 453, 1277–1297. doi:10.1098/rspa.1997.0070.
- Greenwood, J.A., 2017. Reflections on and extensions of the Fuller and Tabor theory of rough surface adhesion. *Tribol. Lett.* 65, 159. doi:10.1007/s11249-017-0938-1.
- Greenwood, J.A., Williamson, J.B.P., 1966. Contact of nominally flat surfaces. *Proc. R. Soc. London, Ser. A* 295, 300–319. doi:10.1098/rspa.1966.0242.
- Griffith, A.A., Taylor, G.I., 1921. VI. The phenomena of rupture and flow in solids. *Philos. Trans. R. Soc. London, Ser. A* 221, 163–198. doi:10.1098/rsta.1921.0006.
- Guduru, P.R., 2007. Detachment of a rigid solid from an elastic wavy surface: Theory. *J. Mech. Phys. Solids* 55, 445–472. doi:10.1016/j.jmps.2006.09.004.
- Guduru, P.R., Bull, C., 2007. Detachment of a rigid solid from an elastic wavy surface: Experiments. *J. Mech. Phys. Solids* 55, 473–488. doi:10.1016/j.jmps.2006.09.007.
- Hertz, H., 1881. Ueber die Berührung fester elastischer Körper. *J. Reine Angew. Math.* 92, 156–171. doi:10.1515/crll.1882.92.156.
- Hockney, R.W., 1970. The potential calculation and some applications, in: Alder, B.A., Fernbach, S., Rotenberg, M. (Eds.), *Methods in Computational Physics*, Vol. 9. Academic Press, New York, pp. 135–211.
- Hulikal, S., Bhattacharya, K., Lapusta, N., 2017. The relation between a microscopic threshold-force model and macroscopic models of adhesion. *Acta Mech. Sin.* 33, 508–515. doi:10.1007/s10409-016-0630-y.
- Irwin, G.R., 1957. Analysis of stresses and strains near the end of a crack transversing a plate. *J. Appl. Mech.* 24, 361–364. doi:10.1115/1.4011547.
- Joanny, J.F., de Gennes, P.G., 1984. A model for contact angle hysteresis. *J. Chem. Phys.* 81, 552–562. doi:10.1063/1.447337.
- Johnson, K.L., 1985. *Contact Mechanics*. Cambridge University Press.
- Johnson, K.L., Kendall, K., Roberts, A.D., 1971. Surface energy and the contact of elastic solids. *Proc. R. Soc. London, Ser. A* 324, 301–313. doi:10.1098/rspa.1971.0141.
- Kesari, H., Doll, J.C., Pruitt, B.L., Cai, W., Lew, A.J., 2010. Role of surface roughness in hysteresis during adhesive elastic contact. *Philos. Mag. Lett.* 90, 891–902. doi:10.1080/09500839.2010.521204.
- Kesari, H., Lew, A.J., 2011. Effective macroscopic adhesive contact behavior induced by small surface

- roughness. *J. Mech. Phys. Solids* 59, 2488–2510. doi:10.1016/j.jmps.2011.07.009.
- Larkin, A.I., Ovchinnikov, Y.N., 1979. Pinning in type II superconductors. *J. Low. Temp. Phys.* 34, 409–428. doi:10.1007/BF00117160.
- Lazarus, V., 2011. Perturbation approaches of a planar crack in linear elastic fracture mechanics: A review. *J. Mech. Phys. Solids* 59, 121–144. doi:10.1016/j.jmps.2010.12.006.
- Lebihain, M., Ponson, L., Kondo, D., Leblond, J.B., 2021. Effective toughness of disordered brittle solids: A homogenization framework. *J. Mech. Phys. Solids* 153, 104463. doi:10.1016/j.jmps.2021.104463.
- Leblond, J.B., Patinet, S., Frelat, J., Lazarus, V., 2012. Second-order coplanar perturbation of a semi-infinite crack in an infinite body. *Eng. Fract. Mech.* 90, 129–142. doi:10.1016/j.engfracmech.2012.03.002.
- Li, Q., Pohrt, R., Popov, V.L., 2019. Adhesive strength of contacts of rough spheres. *Front. Mech. Eng.* 5, 7. doi:10.3389/fmech.2019.00007.
- Liu, S., Wang, Q., Liu, G., 2000. A versatile method of discrete convolution and FFT (DC-FFT) for contact analyses. *Wear* 243, 101–111. doi:10.1016/S0043-1648(00)00427-0.
- Love, A.E.H., 1929. IX. The stress produced in a semi-infinite solid by pressure on part of the boundary. *Philos. Trans. R. Soc. Lond. A* 228, 377–420. doi:10.1098/rsta.1929.0009.
- Maugis, D., 1992. Adhesion of spheres: The JKR-DMT transition using a Dugdale model. *J. Colloid Interface Sci.* 150, 243–269. doi:10.1016/0021-9797(92)90285-T.
- Maugis, D., 2010. *Contact, Adhesion and Rupture of Elastic Solids*. Springer, Berlin; New York. doi:10.1007/978-3-662-04125-3.
- Medina, S., Dini, D., 2014. A numerical model for the deterministic analysis of adhesive rough contacts down to the nano-scale. *Int. J. Solids Struct.* 51, 2620–2632. doi:10.1016/j.ijsolstr.2014.03.033.
- Middleton, A.A., 1992. Asymptotic uniqueness of the sliding state for charge-density waves. *Phys. Rev. Lett.* 68, 670–673. doi:10.1103/PhysRevLett.68.670.
- Monti, J., McGuiggan, P.M., Robbins, M.O., 2019. Effect of roughness and elasticity on interactions between charged colloidal spheres. *Langmuir* 35, 15948–15959. doi:10.1021/acs.langmuir.9b02161.
- Monti, J.M., Sanner, A., Pastewka, L., 2021. Distribution of gaps and adhesive interaction between contacting rough surfaces. *Tribol. Lett.* 69, 80. doi:10.1007/s11249-021-01454-6.
- Muller, V.M., Yushchenko, V.S., Derjaguin, B.V., 1980. On the influence of molecular forces on the deformation of an elastic sphere and its sticking to a rigid plane. *J. Colloid Interface Sci.* 77, 91–101. doi:10.1016/0021-9797(80)90419-1.
- Müser, M.H., 2014. Single-asperity contact mechanics with positive and negative work of adhesion: Influence of finite-range interactions and a continuum description for the squeeze-out of wetting fluids. *Beilstein J. Nanotechnol.* 5, 419–437. doi:10.3762/bjnano.5.50.
- Müser, M.H., 2016. A dimensionless measure for adhesion and effects of the range of adhesion in contacts of nominally flat surfaces. *Tribol. Int.* 100, 41–47. doi:10.1016/j.triboint.2015.11.010.
- Müser, M.H., Dapp, W.B., Bugnicourt, R., Sainsot, P., Lesaffre, N., Lubrecht, T.A., Persson, B.N.J., Harris, K., Bennett, A., Schulze, K., Rohde, S., Ifju, P., Gregory Sawyer, W., Angelini, T., Esfahani, H.A., Kadkhodaei, M., Akbarzadeh, S., Wu, J.J., Vorlaufer, G., Vernes, A., Solhjoo, S., Vakis, A.I., Jackson, R.L., Xu, Y., Streater, J., Rostami, A., Dini, D., Medina, S., Carbone, G., Bottiglione, F., Afferrante, L., Monti, J., Pastewka, L., Robbins, M.O., Greenwood, J.A., 2017. Meeting the contact-mechanics challenge. *Tribol. Lett.* 65, 118. doi:10.1007/s11249-017-0900-2.
- Nocedal, J., Wright, S.J., 2006. *Numerical Optimization*. Springer Series in Operations Research. 2nd ed., Springer, New York.
- Pastewka, L., Robbins, M.O., 2014. Contact between rough surfaces and a criterion for macroscopic adhesion. *Proc. Natl. Acad. Sci. U.S.A.* 111, 3298–3303. doi:10.1073/pnas.1320846111.
- Pastewka, L., Robbins, M.O., 2016. Contact area of rough spheres: Large scale simulations and simple scaling laws. *Appl. Phys. Lett.* 108, 221601. doi:10.1063/1.4950802.
- Pastewka, L., Sharp, T.A., Robbins, M.O., 2012. Seamless elastic boundaries for atomistic calculations. *Phys. Rev. B* 86, 075459. doi:10.1103/PhysRevB.86.075459.
- Patinet, S., Alzate, L., Barthel, E., Dalmás, D., Vandembroucq, D., Lazarus, V., 2013. Finite size effects on crack front pinning at heterogeneous planar interfaces: Experimental, finite elements and perturbation approaches. *J. Mech. Phys. Solids* 61, 311–324. doi:10.1016/j.jmps.2012.10.012.
- Persson, B.N.J., 2002a. Adhesion between an elastic body and a randomly rough hard surface. *Eur. Phys. J. E* 8, 385–401. doi:10.1140/epje/i2002-10025-1.
- Persson, B.N.J., 2002b. Adhesion between elastic bodies with randomly rough surfaces. *Phys. Rev. Lett.* 89, 245502. doi:10.1103/PhysRevLett.89.245502.
- Persson, B.N.J., Scaraggi, M., 2014. Theory of adhesion: Role of surface roughness. *J. Chem. Phys.* 141, 124701. doi:10.1063/1.4895789.

- Persson, B.N.J., Tosatti, E., 2001. The effect of surface roughness on the adhesion of elastic solids. *J. Chem. Phys.* 115, 5597–5610. doi:10.1063/1.1398300.
- Pohrt, R., Popov, V.L., 2015. Adhesive contact simulation of elastic solids using local mesh-dependent detachment criterion in boundary elements method. *Facta Universitatis* 13, 3–10.
- Polonsky, I.A., Keer, L.M., 1999. A numerical method for solving rough contact problems based on the multi-level multi-summation and conjugate gradient techniques. *Wear* 231, 206–219. doi:10.1016/S0043-1648(99)00113-1.
- Ponson, L., 2016. Statistical aspects in crack growth phenomena: How the fluctuations reveal the failure mechanisms. *Int. J. of Fract.* 201, 11–27. doi:10.1007/s10704-016-0117-7.
- Ponson, L., Bonamy, D., 2010. Crack propagation in brittle heterogeneous solids: Material disorder and crack dynamics. *Int. J. Fract.* 162, 21–31. doi:10.1007/s10704-010-9481-x.
- Rey, V., Anciaux, G., Molinari, J.F., 2017. Normal adhesive contact on rough surfaces: Efficient algorithm for FFT-based BEM resolution. *Comput. Mech.* 60, 69–81. doi:10.1007/s00466-017-1392-5.
- Rice, J., 1989. Weight function theory for three-dimensional elastic crack analysis, in: Wei, R., Gangloff, R. (Eds.), *Fracture Mechanics: Perspectives and Directions (Twentieth Symposium)*. ASTM International, 100 Barr Harbor Drive, PO Box C700, West Conshohocken, PA 19428-2959, pp. 29–57. doi:10.1520/STP18819S.
- Rice, J.R., 1985a. First-order variation in elastic fields due to variation in location of a planar crack front. *J. Appl. Mech.* 52, 571–579. doi:10.1115/1.3169103.
- Rice, J.R., 1985b. Three-dimensional elastic crack tip interactions with transformation strains and dislocations. *Int. J. Solids Struct.* 21, 781–791. doi:10.1016/0020-7683(85)90081-2.
- Robbins, M.O., Joanny, J.F., 1987. Contact angle hysteresis on random surfaces. *Europhys. Lett.* 3, 729–735. doi:10.1209/0295-5075/3/6/013.
- Rosso, A., Krauth, W., 2002. Roughness at the depinning threshold for a long-range elastic string. *Phys. Rev. E* 65, 025101. doi:10.1103/PhysRevE.65.025101.
- Rosso, A., Le Doussal, P., Wiese, K.J., 2007. Numerical calculation of the functional renormalization group fixed-point functions at the depinning transition. *Phys. Rev. B* 75, 220201. doi:10.1103/PhysRevB.75.220201.
- Salvadori, A., Fantoni, F., 2014. Weight function theory and variational formulations for three-dimensional plane elastic cracks advancing. *Int. J. Solids Struct.* 51, 1030–1045. doi:10.1016/j.ijsolstr.2013.11.029.
- Schmittbuhl, J., Hansen, A., Batrouni, G.G., 2003. Roughness of interfacial crack fronts: Stress-weighted percolation in the damage zone. *Phys. Rev. Lett.* 90, 045505. doi:10.1103/PhysRevLett.90.045505.
- Schmittbuhl, J., Roux, S., Vilotte, J.P., Jorgen Måloy K, 1995. Interfacial crack pinning: Effect of nonlocal interactions. *Phys. Rev. Lett.* 74, 1787–1790. doi:10.1103/PhysRevLett.74.1787.
- Sneddon, I.N., 1946. Boussinesq's problem for a flat-ended cylinder. *Math. Proc. Cambridge Philos. Soc.* 42, 29–39. doi:10.1017/S0305004100022702.
- Stanley, H.M., Kato, T., 1997. An FFT-based method for rough surface contact. *J. Tribol.* 119, 481–485. doi:10.1115/1.2833523.
- Steihaug, T., 1983. The conjugate gradient method and trust regions in large scale optimization. *SIAM J. Numer. Anal.* 20, 626–637. doi:10.1137/0720042.
- Stormo, A., Gjerden, K.S., Hansen, A., 2012. Onset of localization in heterogeneous interfacial failure. *Phys. Rev. E* 86, 025101. doi:10.1103/PhysRevE.86.025101.
- Tabor, D., 1977. Surface forces and surface interactions. *J. Colloid Interface Sci.* 58, 2–13. doi:10.1016/0021-9797(77)90366-6.
- Tada, H., Paris, P.C., Irwin, G.R., 2000. *The Stress Analysis Of Cracks Handbook*. 3rd ed., ASME Press, New York.
- Tanguy, A., Vettorel, T., 2004. From weak to strong pinning I: A finite size study. *Eur. Phys. J. B* 38, 71–82. doi:10.1140/epjb/e2004-00101-6.
- Thomson, R., Hsieh, C., Rana, V., 1971. Lattice trapping of fracture cracks. *J. Appl. Phys.* 42, 3154–3160. doi:10.1063/1.1660699.
- Violano, G., Afferrante, L., 2021. Roughness-induced adhesive hysteresis in self-affine fractal surfaces. *Lubricants* 9, 7. doi:10.3390/lubricants9010007.
- Vollebregt, E.A.H., 2014. The bound-constrained conjugate gradient method for non-negative matrices. *J. Optim. Theory Appl.* 162, 931–953. doi:10.1007/s10957-013-0499-x.
- Wang, A., Müser, M.H., 2017. Gauging Persson theory on adhesion. *Tribol. Lett.* 65, 103. doi:10.1007/s11249-017-0886-9.
- Wang, A., Zhou, Y., Müser, M.H., 2021. Modeling adhesive hysteresis. *Lubricants* 9, 17. doi:10.3390/lubricants9020017.

- Wei, Z., He, M.F., Zhao, Y.P., 2010. The effects of roughness on adhesion hysteresis. *J. Adhes. Sci. Technol.* 24, 1045–1054. doi:10.1163/016942409X12584625925222.
- Wu, J.J., 2010. The jump-to-contact distance in atomic force microscopy measurement. *J. Adhes.* 86, 1071–1085. doi:10.1080/00218464.2010.519256.
- Xia, S., Ponson, L., Ravichandran, G., Bhattacharya, K., 2012. Toughening and asymmetry in peeling of heterogeneous adhesives. *Phys. Rev. Lett.* 108, 196101. doi:10.1103/PhysRevLett.108.196101.
- Xia, S., Ponson, L., Ravichandran, G., Bhattacharya, K., 2015. Adhesion of heterogeneous thin films II: Adhesive heterogeneity. *J. Mech. Phys. Solids* 83, 88–103. doi:10.1016/j.jmps.2015.06.010.
- Zappone, B., Rosenberg, K.J., Israelachvili, J., 2007. Role of nanometer roughness on the adhesion and friction of a rough polymer surface and a molecularly smooth mica surface. *Tribol. Lett.* 26, 191. doi:10.1007/s11249-006-9172-y.
- Zhou, Y., 2000. Critical Dynamics of Contact Lines. Ph.D. thesis. Johns Hopkins University. Baltimore, Maryland, USA.